Draft version May 28, 2026
Typeset using LaTeX **twocolumn** style in AASTeX631

Climate Patterns of Spin-Orbit Resonant Exoplanets Around Low-Mass Stars

Maria Di Paolo [1], David P. Stevens [1] and Manoj Joshi [2,3]

[1] *Centre for Ocean and Atmospheric Sciences*
School of Engineering, Mathematics and Physics
University of East Anglia
Norwich NR4 7TJ, United Kingdom
[2] *Centre for Ocean and Atmospheric Sciences*
School of Environmental Sciences
University of East Anglia
Norwich NR4 7TJ, United Kingdom
[3] *Climatic Research Unit*
University of East Anglia
Norwich NR4 7TJ, United Kingdom

ABSTRACT

M dwarfs are the most promising candidates for finding habitable worlds through atmospheric characterization. Planets in the habitable zone of low-mass stars experience intense tidal forcings and often become tidally locked. Despite the majority of research being centered on the climate dynamics of synchronously rotating planets in this scenario, synchronous rotation is not an inevitable outcome of tidal locking. Several different circumstances can result in an asynchronous rotation, and in some instances can lead to spin-orbit resonances (SORs). We explore the climates of two different spin-orbit resonant scenarios with a coupled atmosphere-ocean general circulation climate model. Given the crucial role played by the oceans in shaping planetary climate, we adopt two different ocean tidal forcing parameterizations for each SOR scenario. Each of these cases are simulated with both a dynamic ocean and a thermodynamic ocean. Our findings reveal striking differences between the analyzed resonant case and the commonly studied synchronous rotation case. Periodic climate patterns are observed, with climatic features such as clouds and rainfall exhibiting a 60° longitudinal shift relative to the substellar point. The evolution of quantities such as thermal emission and reflected light during a stellar period is noteworthy from the observational point of view, showing appreciable differences compared to the synchronous rotation scenario.

Keywords: Exoplanets (498) — Spin-orbit resonances(2296) — Ocean tides (1152) — Habitable planets (695) — M stars (985) — Planetary climates (2184) — Ocean-atmosphere interactions (1150) — Astrobiology (74) — Exoplanet atmospheres (487) — Planetary atmospheres (1244) — Atmospheric circulation (112) — Atmospheric dynamics (2300)

1. INTRODUCTION

Planets orbiting M- and K- dwarf stars represent the best candidates for detailed characterizations of potentially habitable terrestrial exoplanetary atmospheres using next-generation observatories. Planets orbiting cool stars offer multiple observational benefits, stemming both from the high occurrence rate of these stars and their orbiting planets (Dressing & Charbonneau 2013, 2015; Cloutier & Menou 2020; Ment & Charbonneau 2023) as well as from inherent observational advantages (Scalo et al. 2007; Charbonneau & Deming 2007; Shields et al. 2016). The interest in these systems has catalyzed the development of novel observational techniques and steered mission concepts designed for the forthcoming decade (Kasper et al. 2021; Quanz et al. 2022a; Harada et al. 2024; Zúñiga-Fernández et al. 2024; Angerhausen

Corresponding author: Maria Di Paolo
M.Di-Paolo@uea.ac.uk

et al. 2024). It is therefore imperative to prioritize the integration and application of climate modeling studies to effectively support the observational community in the characterization of potentially habitable exoplanets.

Climate modeling studies of potentially habitable exoplanets have predominantly employed general circulation models (GCMs) with simplified ocean representations, such as slab oceans (Kopparapu et al. 2016, 2017; Boutle et al. 2017; Hammond & Komacek 2024). Thanks to their computational efficiency, these approaches have provided valuable insights into planetary habitability, atmospheric processes and surface characteristics through parameter sweeps (Kopparapu et al. 2017; Kilic et al. 2017; Nowajewski et al. 2018; Komacek & Abbot 2019). However, these studies inherently limit the accuracy of climate and habitability assessments, as they do not account for the complex interactions and feedbacks associated with fully dynamic oceans. The crucial role of ocean circulation, and therefore ocean heat transport, in stabilizing Earth's climate by mitigating geographic, seasonal, and diurnal temperature extremes is well studied (Trenberth & Caron 2001; Winton 2003; Herweijer et al. 2005). Studies conducted over the last fifteen years substantiate that ocean dynamics constitute a significant contribution to climate studies across a variety of planetary contexts, encompassing Earth's paleoclimates (Yang et al. 2012a,b; Kienert et al. 2012; Ragon et al. 2024), climate simulations of planets orbiting in the early Solar System (Way & Del Genio 2020; Schmidt et al. 2022), and exoclimes (Hu & Yang 2014; Cullum et al. 2014; Kilic et al. 2018; Olson et al. 2020). In general, although the assumption of a simplified ocean is certainly computationally convenient, the potential underestimation/misrepresentation of certain processes and feedbacks can lead to a failure to capture key climatic features, hence why fully coupled AOGCMs represent the most physically comprehensive tools for fully characterizing terrestrial climate (Yang et al. 2013; Hu & Yang 2014; Ferreira et al. 2014; Kilic et al. 2018; Yang et al. 2019; Di Paolo et al. 2025).

The interest in characterizing habitable planets around cool stars is long-standing, but poses several challenges from both the observational and the theoretical point of view. The prospect of building accurate climate models is hindered by the fact that many characteristics of planets in this configuration are ultimately unknown, such as their spin state. Due to the low luminosity of cool dwarfs, the circumstellar habitable zone in such systems is located relatively close to the host star (Kasting et al. 1993; Kopparapu et al. 2013). Consequently, potentially habitable planets orbiting in these systems experience strong tidal interactions, which can alter the planet's rotational angular momentum through a process known as tidal locking (Murray & Dermott 1999). While tidal locking and its possible outcomes have been studied since the 1960s in the context of Solar System planets and satellites (MacDonald 1964; Goldreich 1965; Goldreich & Peale 1966a,b; Goldreich 1966), tidal studies for exoplanets are challenging due to a combination of observational limitations - such as sparse constraints on the orbital architecture of the system and the presence of companions - and uncertainties in planetary properties - such as atmospheric structure, internal and rheological variables, tidal deformation and dissipation parameters.

Possible outcomes of such tidal evolution in this scenario seem to be manifold, ranging from spin-orbit resonances (SORs) to librations of different amplitude and even chaotic behaviour (Dobrovolskis 2007; Leconte et al. 2015; Vinson & Hansen 2017; Barnes 2017; Renaud et al. 2021; Chen et al. 2023; Valente et al. 2024; Yuan et al. 2025). The most commonly studied scenario is a special case of tidal locking: the 1:1 SOR, or synchronous rotation, where the periods for the planet to complete one rotation on its spin axis and one orbit around the host star are identical, giving a permanent dayside and nightside. Atmospheric heat transport can prevent nightside volatile trapping for reasonable values of surface pressure (Joshi et al. 1997), while ocean heat transport can extend an "eyeball" state, with a pool of open water centered on the substellar point (Pierrehumbert 2011), into a "lobster" (Hu & Yang 2014). Several studies have analyzed different aspects of climates in this scenario, focusing mainly on distinct regimes of atmospheric circulation depending on the planetary rotation period, atmospheric composition, surface pressure, incident stellar flux, surface gravity, planetary radius, and cloud particle size (e.g., Kopparapu et al. (2017); Haqq-Misra et al. (2018); Komacek & Abbot (2019)).

Only a few studies have focused on higher order resonances, among which the 3:2 SOR is the lowest order non-synchronous resonance and the most likely to occur for low values of orbital eccentricity (Correia & Laskar 2009). In this case, the planet rotates three times on its spin axis for every two orbits it completes around its host star, meaning that the substellar point shifts by 180° in longitude for every completed orbit (see Figure 1).

Climate simulations of GJ 667Cc for an orbit with eccentricity 0.4 and several SORs, assuming a slab ocean and thermodynamic sea ice, found two distinct patterns of the mean state climate: an "eyeball" exoplanet with a substellar warm region (1:1, 2:1 SORs) and a "waterbelt" exoplanet with zonally uniform temperature

decreasing with latitude (3:2, 5:2 SORs) (Wang et al. 2014). Thermal phase curves can be used to distinguish between these two climate patterns, with the former presenting significantly stronger variations than the latter during an orbital period. However, Dobrovolskis (2015) later proved that they used incorrect spatial insolation functions for the 3:2 and 5:2 resonances, and that for an eccentric orbit these SORs would result in a "double-eyeball" pattern rather a "waterbelt" exoplanet.

The climate of Proxima b has been the subject of several investigations that compare the 1:1 and 3:2 scenarios in the case of circular and/or eccentric orbits with either a static ocean (Turbet et al. 2016; Boutle et al. 2017) or a shallow dynamic ocean (Del Genio et al. 2019). The results are generally similar, with the 3:2 SOR climates exhibiting large meridional temperature gradients, with an equatorial "waterbelt" configuration that can transition to a "double-eyeball" configuration with increasing eccentricity. These results are highly sensitive to the choice of parameters such as the instellation and the chosen albedo, which ultimately determine the presence of open-water regions as opposed to a "slushball" planet. When a dynamic ocean is considered, the peak ocean surface temperature occurs slightly downstream with respect to the substellar point, due to modest eastward ocean heat transport at this location (Del Genio et al. 2019). Moreover, the atmospheric circulation in the null eccentricity case is similar to that of a moderately slowly rotating Earth, with Hadley cells extending to the poles, westerly jets in the midlatitudes, easterly trade winds at low latitudes and a very weak westerly equatorial surface ocean current (Del Genio et al. 2019). More recently, Braam et al. (2025) used a 3D coupled climate-chemistry model to study Proxima b for circular 1:1 and eccentric 3:2 SORs. Synthetic mid-infrared spectra showed that the severe zonal asymmetries of the 1:1 SOR case lead to spectral fluctuations as a function of orbital phase, which are dampened in the 3:2 SOR case because of the more homogeneous atmosphere.

More general results, not tied to a specific exoplanet, include a study of the effect of sea ice drift on snowball transitions at the outer edge of the habitable zone, performed with a fully coupled atmosphere-ocean-sea ice model for a sample of nine exoplanets (Yang et al. 2020). By conducting an array of sensitivity tests for a range of parameters, they found that sea-ice drift is efficient in shrinking the open ocean and leading the system to a snowball state. Another more generalized study employed a 3D GCM with a shallow dynamic ocean and incorporated tidal heating to model SOR exoplanets at the inner edge of the habitable zone, showing that internal heating drives a rapid transition from temperate to moist greenhouse states, with only minor effects on upper atmospheric water mixing ratios (Colose et al. 2021). To date, 3:2 SOR climate studies have primarily focused on the mean climate state, and, to our knowledge, no AOGCM investigation of climate pattern variability over a stellar period has yet been conducted.

In this study, we investigate the climate of ocean worlds in 3:2 SORs orbiting cool host stars with the FORTE2.0 AOGCM (Blaker et al. 2021). Differently from previously published studies, we use a custom continental "Ridgeworld" configuration (see Methods). Rather than concentrating on a single, specific exoplanet, our goal is to conduct a broadly applicable study, providing insights into potentially common features of exoclimes in this scenario. Accordingly, we investigate two different rotation and orbital periods, and consider two different ocean tidal scenarios, since both of these phenomena have significant effects on planetary climate (Cullum et al. 2014; Di Paolo et al. 2025). We present an in-depth analysis of several climate features in this scenarios, both for the ocean and the atmosphere. We finally present simulated phase curves of planetary thermal emission, which reveal a potential discriminant to determine whether a planet is characterized by either a 1:1 or a 3:2 SOR state.

2. METHODS

2.1. *Model description*

FORTE 2.0 (Blaker et al. 2021) is a fast and flexible coupled AOGCM of intermediate-resolution. The ocean general circulation model (Modular Ocean Model – Array Processor, or MOMA) (Webb 1996) is coupled once per model day to the atmospheric general circulation model (Intermediate Global Circulation Model version 4, or IGCM4) (Joshi et al. 2015).

In the MOMA setup adopted here, horizontal resolution is $2^\circ \times 2^\circ$, with 15 vertical z-layer levels. Level thickness increases progressively with depth, from 30 m at the surface to 836.10 m at depth. Overall, the ocean extends to a depth of approximately 5500 m.

The IGCM4 setup is characterized by a T42 spectral resolution, a grid spacing of $\sim 2.8^\circ$, and a troposphere-only atmosphere, extending to about 25 km in altitude, subdivided into 20σ levels.

The convection scheme and stratiform precipitation in the IGCM4 are mostly based on Forster et al. (2000), with a few additional parameterisations and adjustments to better match observations of Earth (Joshi et al. 2015).

2.2. *System architecture*

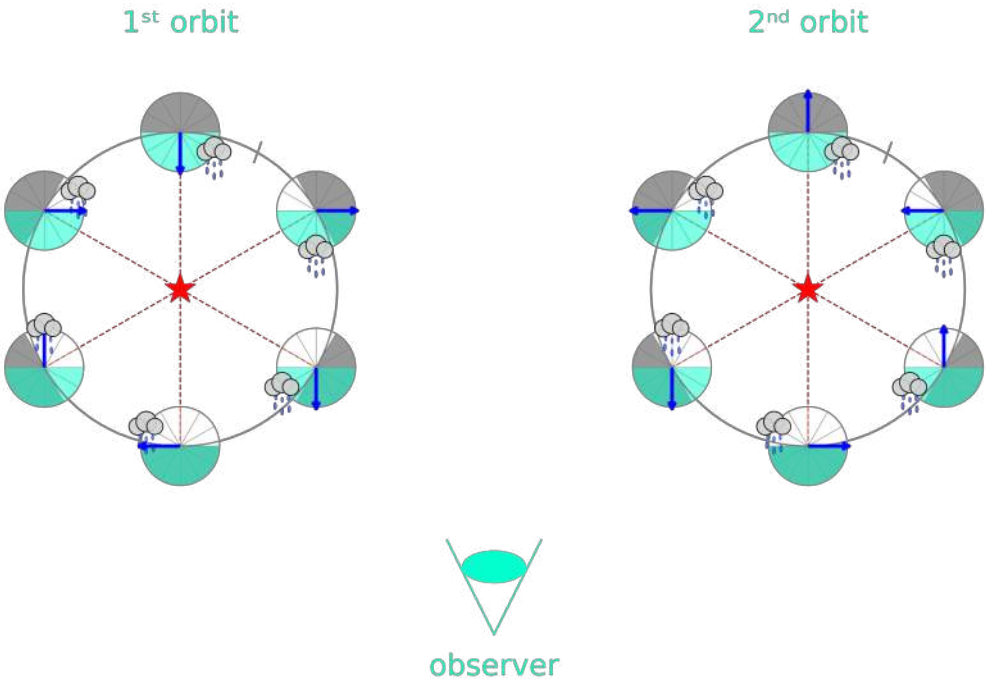

Figure 1: Observing configuration, assuming both an anticlockwise orbit and an anticlockwise spin rotation. **The planetary orbit is edge-on, with the observer in the plane of the paper.** White/gray hemispheres represent the day/night sides at each point of the orbit. **The turquoise hemispheres represent the observable portion of the planet within the observer's field of view: regions theoretically observable in reflected light correspond to the portions where the turquoise hemisphere and the white hemisphere overlap, whereas regions theoretically observable in emitted light encompass the entirety of the turquoise hemispheres.** The blue arrow is a reference meridian. The substellar point, positioned in correspondence of the red dashed line on the planetary surface, shifts 180° in longitude for every completed orbit, realigning with its initial location after two full orbits (or one stellar period).

We choose two representative M stars in the range of masses of the spectral class, $M_\star \approx (0.08 - 0.6)\, M_\odot$, where $M_\odot$ is the solar mass (see Table 1). We assume an Earthlike stellar radiation forcing at the top of the atmosphere, with $S_\odot = 1365$ Wm^{-2}. For simplicity, the planetary orbit is modeled to be circular, with null orbital inclination, thus edge-on with respect to the hypothetical observer, and the planetary axial tilt is zero.

The choice of a null eccentricity is motivated by a number of reasons. While equilibrium tide theory states that a non-zero orbital eccentricity is required for a planet not to be captured into 1:1 SOR, but rather into higher order resonances, theoretical studies are usually limited to considering tidal interactions between a planet and its host star, neglecting the possibility of additional forcings due to planetary companions or satellites, or even disturbances linked to impacts, and generally have a restricted treatment of rheology and planetary triaxiality.

Planetary systems around M dwarfs are often multiple and tightly dynamically packed (Fang & Margot 2013; Ballard & Johnson 2016). Thus, planetary spin states might be significantly influenced by gravitational interactions between neighbouring planets. Provided a companion is present in the system, asynchronous SORs are possible even when the eccentricity is nearly zero (Correia & Delisle 2019). For instance, Vinson & Hansen (2017) demonstrated that interactions between Earth-sized planets near a mean motion resonance are strong enough to lead to high amplitude librations of the spin state, or even complete circulation, instead of 1:1 SORs.

Moreover, a number of transit timing variations studies estimate small eccentricities ranging from 0.01 to 0.1 for the majority of low-mass planetary systems (Wu & Lithwick 2013; Van Eylen & Albrecht 2015; Hadden & Lithwick 2017). Multiple investigations of the climate of Proxima b in a 3:2 SOR state assumed a null orbital eccentricity, justifying this choice on the fact that an eccentricity of about ~ 0.06 would be sufficient to capture the planet into a 3:2 SOR (Ribas et al. 2016).

In order to determine the orbital radius in each case, and therefore the orbital period, we express the instellation received by the modeled exoplanet $S_\star$ in terms of $L_\star$, the luminosity of the host star in solar units ($L_\odot$),

and $r_{p,\star}$, the planetary orbital radius in au units. Adopting a traditional parametrization of the luminosity-mass relationship (Harwit 1998) yields:

$$S_\star = \frac{L_\star}{{r_{p,\star}}^2} = \frac{{M_\star}^{3.5}}{{r_{p,\star}}^2} \quad . \tag{1}$$

We require the instellation received by the modelled exoplanet $S_\star$ to be equal to the insolation that Earth receives, determining the distance between the exoplanet and its host star:

$$\begin{aligned} r_{p,\star} = \sqrt{\frac{{M_\star}^{3.5}}{S_\star}} &\approx (0.05 - 0.13)\sqrt{\frac{{M_\odot}^{3.5}}{S_\odot}} \quad , \\ &\approx (0.05 - 0.13) \text{ au} \quad , \end{aligned} \tag{2}$$

where we substituted the chosen values of the M star mass (see Table 1). Kepler's third law yields the planetary orbital period $T_{orbital}$ in both cases, and by using the values for the host star mass and the planetary orbital radius we obtain:

$$\begin{aligned} T_{orbital} = \sqrt{\frac{4\pi^2 {r_{p,\star}}^3}{GM_\star}} &\approx (0.025 - 0.083)\sqrt{\frac{4\pi^2 {r_{\oplus,\odot}}^3}{GM_\odot}} \quad , \\ &\approx (9 - 30) \text{ days} \quad , \end{aligned} \tag{3}$$

with the subscript $\oplus$ denoting quantities referring to Earth (e.g., $r_{\oplus,\odot}$ for the average orbital radius). We note that, throughout this work, the unit of measure "day" refers to an Earth day.

Since we are modeling 3:2 SOR asynchronously rotating planets, this means that the length of an exoplanet day $T_{rotation}$ can be determined from its orbital period:

$$T_{rotation} = 2/3\ T_{orbital} = (6 - 20) \text{ days} \quad . \tag{4}$$

The stellar day, equivalent of the solar day on Earth, can be computed according to:

$$T_{stellar} = \left(\frac{1}{T_{rotation}} - \frac{1}{T_{orbital}}\right)^{-1} = (18 - 60) \text{ days} \quad , \tag{5}$$

and corresponds to the interval of time between two successive transits of the star across the same reference meridian on the planet.

A simple rendition of this configuration is presented in Figure 1. The reference meridian (blue arrow) realigns with the host star after completing two full orbits, or equivalently after completing three full rotations with respect to the planetary spin axis. Spin-orbit resonance states affect the orbital spatial distribution of incident stellar flux: given that we chose to adopt a null eccentricity all longitudes receive the same amount of stellar flux during a stellar period, unlike the 1:1 SOR and the 3:2 eccentric cases (Dobrovolskis 2015).

	$M_\star$ ($M_\odot$)	$a_{p,\star}$ (au)	$T_{orbital}$ (day)	$T_{rotation}$ (day)	$T_{stellar}$ (day)
Case 1	0.18	0.05	9	6	18
Case 2	0.31	0.13	30	20	60

Table 1: SORs scenarios (the unit of measure "day" is an Earth day).

The simulated climates reach a quasi steady state after 2500 years. The analysis focuses on the last 100 stellar periods after a 2500 year run.

2.3. *Planet configuration*

We consider an Earth-sized ocean planet, covered by a single, global-scale ocean basin of uniform depth (∼5500 m). We adopt a "Ridgeworld" configuration (e.g. Smith et al. (2006); Ferreira et al. (2010); Yang et al. (2019); van de Velde et al. (2021)): a single, 2° wide, meridional ridge 145m below the surface connects two polar islands that extend to 86°N/S. This continental configuration, more general than assuming a specific land mask, importantly allows the formation of ocean gyres, prevents the formation of unrealistically large zonal oceanic jets that occur in "Aquaplanet", while at the same time supporting a large-scale overturning circulation and heat redistribution. The atmospheric composition is Earth-like, characterized by pre-industrial atmospheric concentrations of CO_2.

Asynchronously rotating potentially habitable planets reside in close orbit round their low-mass host stars, experiencing strong tidal interactions. Therefore, they are subjected to large travelling tides. These tidal effects can be parameterized with an enhanced oceanic vertical diffusivity κ (Di Paolo et al. 2025). We choose to analyze SOR scenarios in two different tidal regimes: a low vertical diffusivity regime with $\kappa = 1.5 \times 10^{-4}\text{m}^2\text{s}^{-1}$, similar to the one estimated for Earth $\kappa_\oplus = 1 \times 10^{-4}\text{m}^2\text{s}^{-1}$ (Munk & Wunsch 1998), and a high vertical diffusivity regime with $\kappa = 150 \times 10^{-4}\text{m}^2\text{s}^{-1}$, that corresponds to a maximized total and oceanic heat transport (Di Paolo et al. 2025).

Simulating exoplanetary climate using both a dynamic and a thermodynamic ocean provides critical insight into the role of oceanic processes in regulating planetary climates. For the former, we employ the default setting of MOMA, which is inclusive of both diffusive and advective processes at play in determining the state of the

ocean, while for the latter we adapt MOMA to exclude advection.

The albedos of snow and ice decrease progressively at longer wavelengths, especially beyond 1 μm, due to their optical properties. Low-mass stars emit a substantial portion of their radiation in this longer-wavelength range. The resulting albedos of snow and ice on planets orbiting M-stars are significantly lower than those observed on Earth (Joshi & Haberle 2012). In order to take this into account, we use 0.4 as the maximum value for the ice and snow albedo, consistent with a mean value of calculated albedos for different mixtures of ice and snow (Shields et al. 2013).

3. RESULTS

3.1. *Ocean*

The thermal inertia of the ocean causes the location of the warmest water in the upper layers to be shifted away from the substellar point (Figure 2). At any fixed location, there is a temporal lag between the star's transit overhead and the peak in sea surface temperature. Differently from the synchronous rotation scenario, where the hot spot is fixed on the planetary surface with respect to the substellar point, in this scenario the hot spot travels across the planetary surface following the passage of the star overhead.

The ocean state is tightly linked to the value of κ. As oceanic diffusion becomes more important, the thermocline deepens. Figure 2 shows how, for both rotational states, the signal travels to greater depths in the cases of enhanced κ with respect to their counterparts. This is evident in Figure 3, which shows the temperature profiles in the equatorial band (between latitudes of 5°S and 5°N) at the longitude 120°, with the spread in the upper ocean representing the variability of temperature due to the transient signal. Both the dynamic and the thermodynamic ocean models simulate less stratified profiles in the cases of high κ. In general, the thermodynamic ocean runs exhibit warmer temperatures than the dynamic ocean runs at this location, as when ocean dynamics are active cold water is advected at depth from high latitudes. This has a less evident effect on near surface temperatures, given that the stellar forcing dominates, resulting in generally similar temperatures for both types of ocean model. Only the $T_{orbital} = 30$ days, $\kappa = 1.5\ \kappa_{\oplus}$ scenario presents marginally warmer temperatures near the surface in the case of the dynamic ocean. This is caused by downwelling occurring at the equator which warms the upper ocean layers.

In the case of the dynamic ocean, the ocean response is a combination of a downward propagating signal and dynamical waves that depend on boundary conditions. Figure 4 shows the density anomaly at a depth of about 500 m in the case of the dynamic ocean. The plots on the right are obtained by compositing over one hundred stellar periods in each case. In the high κ cases, the effect of vertical diffusion clearly dominates, resulting in an evident downward propagating signal that is linked to, but lags, the location of the substellar point in time. Taking as a reference the longitude 120°, the position of less/more dense water roughly corresponds to the position of the warmer/colder water depicted in Figure 2 at the same depth.

In the faster rotation case, the temperature anomalies propagate at depth more quickly than in the slower rotation case, which is indicated by the inclination of the black contours in Figure 2. This explains why the density anomalies depicted in Figure 4 seem to be in opposite phases in the two high diffusion cases with different rotation period.

In the low κ cases the downward propagating signal is weaker and shallower, and dynamical features can dominate. In the $T_{orbital} = 9$ days scenario, the very weak intermittent wave-like pattern depicted in Figure 4 appears only after compositing over one hundred stellar periods, but is absent when averaging over shorter intervals of time, and does not appear to be phase-locked with the forcing. Conversely, the bigger anomalies associated with stronger forcing in the $T_{orbital} = 30$ days scenario are westward propagating equatorial Rossby waves and eastward propagating Kelvin waves. These waves originate at the barrier, positioned at longitude 240°, and are triggered by alternating convergence and divergence of zonal winds: converging winds force downwelling of lighter water, while diverging winds force upwelling of denser water. The patterns of winds are described in more detail in the next section (Atmosphere). We further investigate this case by spreading the composited stellar period, obtained by compositing over 100 stellar periods, into 10 stellar periods obtained by compositing over 10 stellar periods (plot on the left of Figure 4). The Rossby waves, spanning the planet with a velocity of about 2 ms^{-1}, are still clearly visible. Multiple and frequent Kelvin waves with a velocity of about 6 ms^{-1} - about three times the Rossby wave speed - are possibly triggered by stochastic forcings such as random weather events. Phase-locked Kelvin waves are more evident east of the barrier when averaging over longer periods of time.

3.2. *Atmosphere*

Figure 5a clearly shows that at all times, the surface temperature peaks with a longitudinal shift of about $\sim 60°$ eastward with respect to the location of the sub-

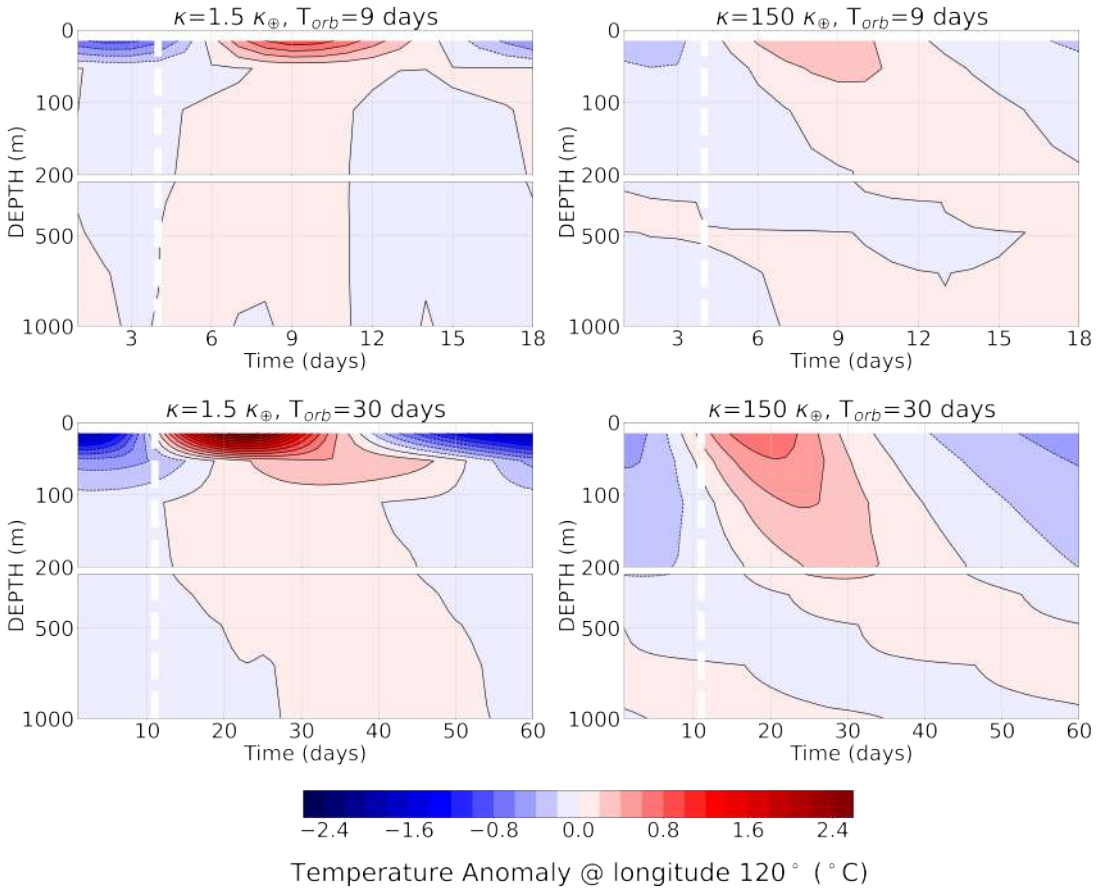

Figure 2: Cross section of the upper dynamic ocean layers, at longitude 120° and between latitudes of 5°S and 5°N, showing temperature anomaly. White dashed lines represent the location of the substellar point. Composite quantities have been averaged over the last 100 stellar periods.

stellar point on the planetary surface, consistent with Figure 2. The most prominent features are observed in the case $T_{orbital} = 30$ days with $\kappa = 1.5\ \kappa_\oplus$, with a higher surface temperature range. In general, scenarios characterized by the same value of the vertical diffusion coefficient will present a stronger signal for the slow rotation scenario (Figure 2 and Figure 5a). In these scenarios, the stellar forcing travels slowly across the surface, the host star illuminates the same spot on the planet for longer periods of time, and the effect of stellar forcing dominates. Scenarios characterized by the same rotation period will present a stronger signal for the low diffusion scenario, as warm water at the surface is not rapidly diffused downwards, and more heat is retained in the upper ocean.

In all scenarios, the effect of surface heating dominates, with moisture building up in the lower atmosphere and condensing into clouds, triggering rainfall. Rainfall peaks with a $\sim 60°$ longitudinal shift with respect to the substellar point (see Figure 5b), coincident with the highest surface temperature. The rainfall is significantly more intense in the case $T_{orbital} = 30$ days with $\kappa = 1.5\ \kappa_\oplus$, associated with the stronger temperature forcing, reaching a maximum of ~ 30 mm day^{-1} over the equatorial band. Rainfall exhibits significant variability over each stellar period. At any fixed location, while the passage of the star overhead is followed by a clear maximum in the signal averaged in time, the non-composited signal is noisy. An example of this is shown in Figure 6, for the longitude $\sim 120° \pm 10°$ in the equatorial band. As expected, the signal to noise ratio increases for slower rotations, where a general similar behaviour is maintained even for the non-averaged signal. The case $T_{orbital} = 30$ days with $\kappa = 1.5\ \kappa_\oplus$ presents the most consistent peak in rainfall for each stellar period, with an average maximum value of ~ 22 mm day^{-1} at this specific location, as expected from the biggest temperature contrast observed in this scenario. The above shift in surface temperature, and consequently in rainfall, is generally observed with both the dynamic and the thermodynamic ocean models.

The surface temperature in the equatorial band is higher in the thermodynamic ocean scenario for all cases except the $T_{orbital} = 30$ days with $\kappa = 1.5$ case, which

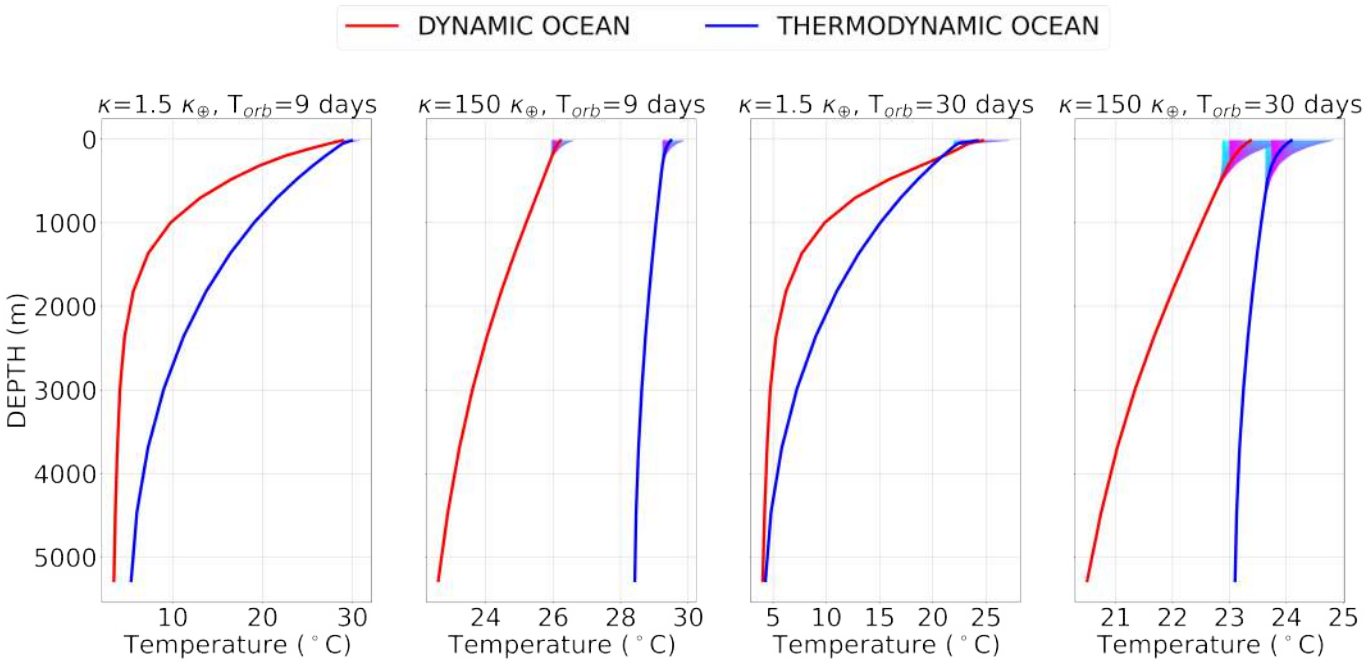

Figure 3: Temperature profiles of dynamic vs thermodynamic ocean at longitude 120° and between latitudes of 5°S and 5°N. For each profile, a spread of daily averaged temperatures is plotted, showcasing the variability of the temperature in the upper ocean layers with the shifting position of the substellar point.

exhibits slightly warmer temperatures in the dynamic ocean scenario, associated with more abundant rainfall. The peak in total rainfall is generally sharper in the case of the thermodynamic ocean than in that of the dynamic ocean. In particular, the higher diffusion scenarios show a bigger relative increase in the maximum value of total rainfall, in accordance with a bigger relative increase in surface temperature (see Figure 3). In general, the signal still exhibits significant variability with time even in the thermodynamic ocean cases. The distribution of clouds, not shown here, does not perfectly correspond to the rainfall pattern. This is due to a delay between the formation of clouds and highest precipitation. At any instant, significant shallow convection is present westward of the substellar point.

Figure 7a depicts the convergence/divergence of equatorial zonal winds through the alternating bands of easterly and westerly winds. As mentioned in the previous section, equatorial zonal winds at 850 hPa generally converge towards the hot spot on the planetary surface, and diverge from the diametrically opposite point. This pattern is evident for the slow rotation cases, while is less demarcated in the faster rotation cases, as a consequence of the weaker surface temperature gradients associated with the position of the substellar point.

The interactions of the wind patterns with the barrier triggers oceanic Rossby (Kelvin) waves that propagate westward (eastward) from the barrier at depth (Figure 4). Observing the case $T_{orbital} = 30$ days with $\kappa = 1.5\ \kappa_\oplus$ at the location of the barrier (longitude 240°), the convergence of eastward and westward zonal winds at the beginning of the stellar period (Figure 7a) results in oceanic downwelling. The warmer lighter water in the upper layers of the ocean is forced downwards into deeper layers ocean, resulting in the negative anomaly depicted in Figure 4. At the same location, about halfway through the stellar period, the divergence of westward and eastward zonal winds (Figure 7a) results in oceanic upwelling. Cold dense water residing at depth is forced upward, leading to a positive anomaly. The anomalies then propagate westward as Rossby waves and eastward as Kelvin waves.

Figure 7b depicts the zonal wind at 850 hPa at the fixed location of 120° as a function of latitude. As expected, the wind at the equator exhibits alternating eastward and westward directions depending on the time during the stellar period. The pattern is more latitudinally extended in the slow rotation scenarios, while it is constrained to lower latitudes in the fast rotation cases owing to weaker divergence associated with a smaller heating anomaly. For the same rotation rate, $\kappa = 150\ \kappa_\oplus$ cases exhibit weaker high-latitude westerlies than $\kappa = 1.5\ \kappa_\oplus$ cases, due to reduced meridional temperature gradients. This behaviour can be described as a moving Walker circulation that follows the shifting position of the peak surface temperature. Similarly, in

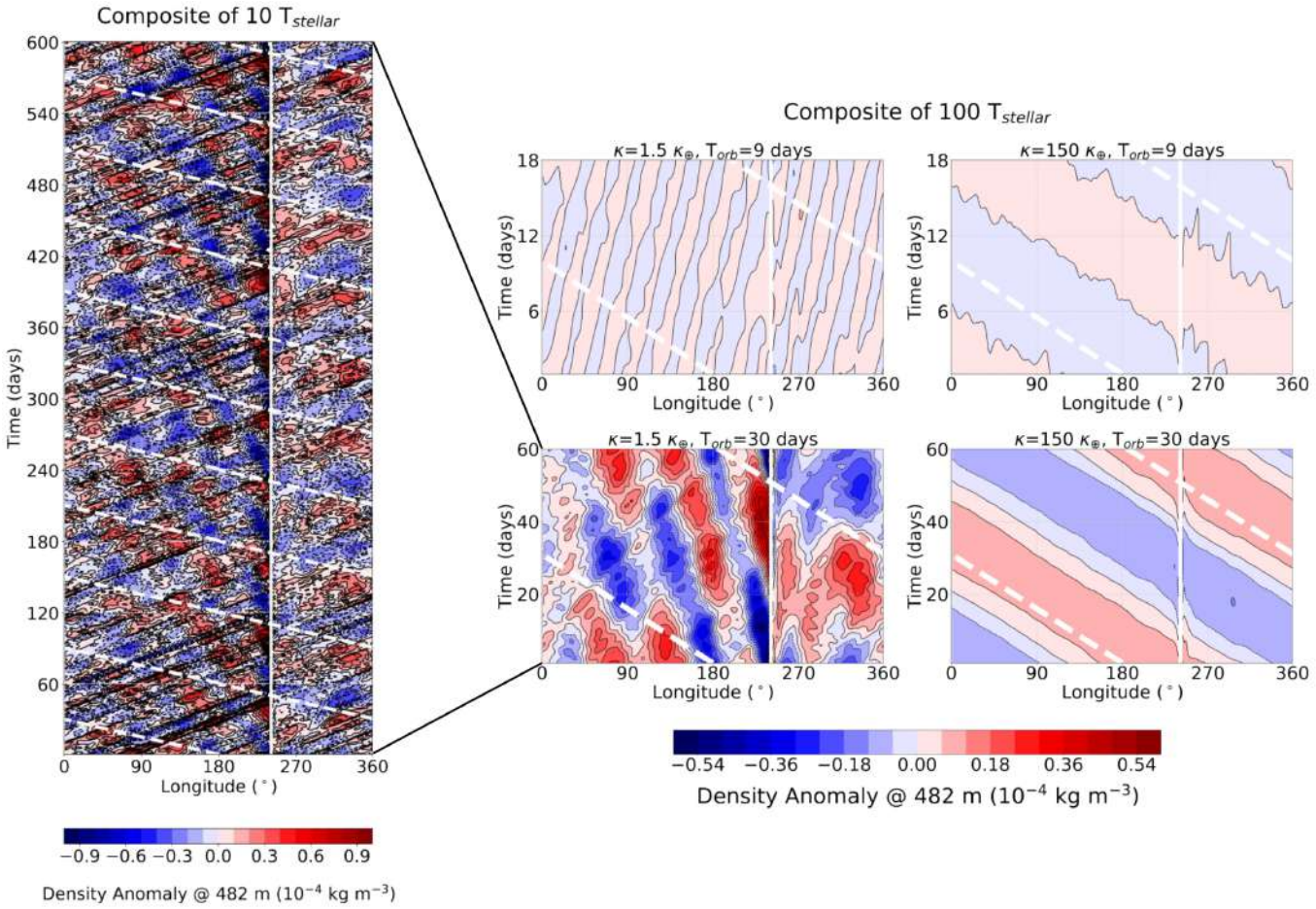

Figure 4: Hovmöller diagram showing density anomaly at 482 m of depth, between latitudes of 5°S and 5°N. White dashed lines represent the location of the substellar point. Composite quantities at the equator have been averaged either over the last 100 stellar periods either into one composited stellar period (plots on the right) or into ten composited stellar periods (plot on the left).

the case of slowly rotating 1:1 SOR exoplanets, atmospheric circulation models predict a global overturning circulation centered on the substellar point; air rises at the substellar point in the permanent day hemisphere, travels towards the colder night hemisphere in the upper atmosphere, and sinks at a location that depends on the strength of the circulation (Hammond & Lewis 2021). Equatorial zonal winds at 250 hPa (not shown) have a superrotating westerly wind jet in all scenarios. In general, the results of the thermodynamic ocean simulations show a similar behaviour. However, asymmetries with respect to the equator and/or with respect to the position of the substellar point depicted in Figure 7 are introduced by dynamical features that are obviously absent in the case of the thermodynamic ocean.

In slow rotation cases, the meridional circulation in the hemisphere centered on the hot spot on the planetary surface consists of a single Hadley cell extending from the equator to the poles (Haqq-Misra et al. 2018), whereas in fast rotation cases the Hadley circulation is restricted to low latitudes.

3.3. *Observables*

Mapping terrestrial exoplanets involves constraining temporal and spatial properties in order to gain further insight into the planetary characteristics, therefore allowing us to develop an understanding of their climate dynamics. Possible photometric signals are the planetary top-of-atmosphere outgoing longwave radiation, or thermal emission, and the top-of-atmosphere outgoing shortwave radiation, or reflected light. Thermal orbital phase curves are a simple method to infer information regarding the planetary temperature and heat transport efficiency from the disk-integrated emitted thermal flux. On the other hand, reflected light orbital phase curves provide crucial insight into surface composition and cloud coverage. Together, photometric phase curves are crucial for understanding exoplanetary climate dynamics and potential habitability.

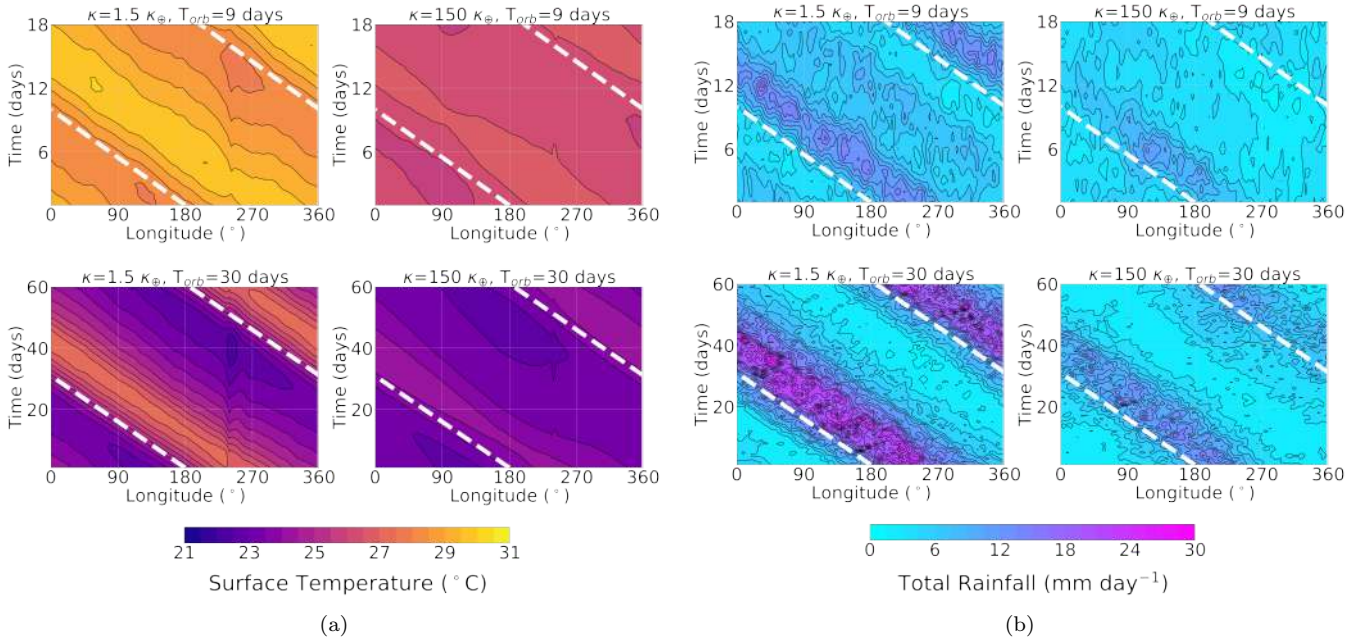

Figure 5: Hovmöller diagram showing composite quantities averaged over the equatorial band (5°S - 5°N) and over the last 100 stellar periods. White dashed lines represent the location of the substellar point. (a) Surface temperature, (b) total rainfall.

The planet top-of-atmosphere outgoing radiation is split into longwave (> 4 μm) **and shortwave (UV-Vis-NIR, between** $0.12 - 0.4$ μm**)** in the atmospheric model output. We assume an edge on orientation, so that orbital phases of ± 0.5 correspond to secondary eclipses, where only the day hemisphere of the planet is visible to the observer, and orbital phases of $\pm 0, 1$ are transit events, where only the night hemisphere of the planet is visible to the observer. In order to focus on the climatic features of each case, we exclude the contribution of the star to the total observed flux in each orbital configuration, effectively separating the planetary signal. The light curves depicted in this section in Figure 9 simulate daily observations for a total of 1800 days, corresponding to 100 stellar period for the faster rotation cases, and 30 stellar periods for the slow rotation scenario. Each plot show the daily visible hemisphere integrated flux, the 10th and 90th percentile and the composited signal.

Previous studies of 3:2 SORs circular orbits scenarios adopted an "Aquaplanet" setup with no meridional barriers, which is completely zonally uniform. Observing different areas of the planet would not imply any longitude-specific feature: excluding transient events, the potential observables would not exhibit any variability between consecutive orbits. In our modelling configuration, it is crucial to consider the full orbital phase curves over two consecutive orbits, or equivalently over one full stellar period. This is because in two consecutive orbits, the same orbital configuration is associated with different portions of the planet in the field of view of the observer. The configuration depicted in Figure 1 shows how the position of a reference meridian (blue arrow) with respect to the observer changes in time: when considering equivalent orbital phases for consecutive orbits, the observed signal originates from different portions of the planet. The white transparent bands in Figures 8 highlight the planetary hemisphere that is visible to the observer at all times during a stellar period.

The top-of-atmosphere shortwave radiation represented in Figure 8 exhibits a slight asymmetry with respect to the substellar point (white dashed line) in all cases: the signal peaks eastward from the position of the substellar point, as we would expect from the previous considerations regarding the rainfall longitudinal shift. The reasons for the small amount of asymmetry because the amount of reflected light is highly dependent on the cloud amount. As mentioned in the previous section (see Atmosphere), the significant asymmetry in the rainfall signal with respect to the substellar point does not necessarily correspond to an equally evident asymmetry in the cloud coverage. The second reason stems from system geometry: incoming stellar flux scales with the cosine of the zenith angle, so the amount of potentially reflected light decreases moving longitudinally away from the substellar point. Although the precipitation peak is

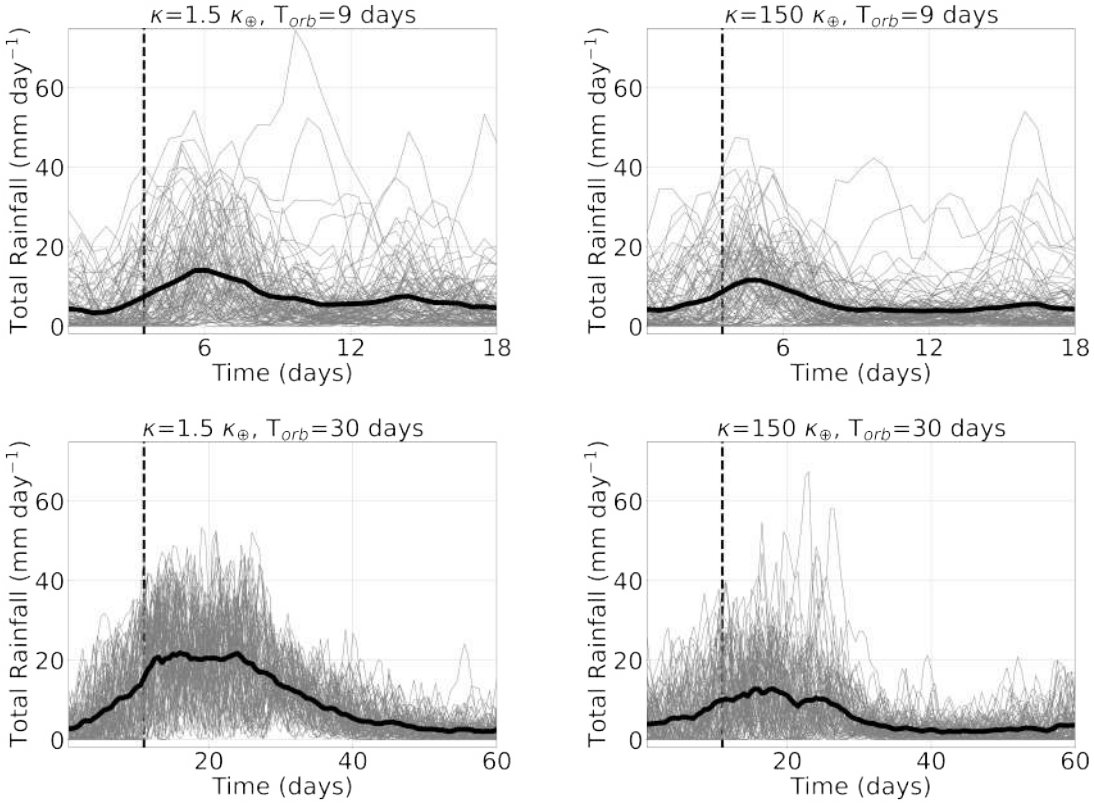

Figure 6: Variability of total rainfall at longitude 120° and averaged between latitudes of 5°S and 5°N. For each case, the thick black solid line represent the composited average over the last 100 stellar periods, while light gray solid lines represent rainfall during each of these stellar periods. Black dashed lines represent the instant that corresponds to the passage of the star overhead at this location.

evident, its $\sim 60°$ offset implies a reduced reflected flux. Consequently, while Figure 8a shows slight asymmetry, the disc-integrated signal in Figure 9 remains largely symmetric about transits/secondary eclipses midpoints, with only minor deviations in slow rotation cases.

The top-of-atmosphere longwave radiation represented in Figure 8b clearly shows that the minimum thermal emission to space is co-located with the maximum rainfall, as the latter is associated with deep convective cloud having cold cloud tops. As expected, the equatorial band signal is more prominent for the $T_{orbital} = 30$ days with $\kappa = 1.5\ \kappa_{\oplus}$ case, that exhibits the strongest rainfall signal. The thermal emission appears to be generally more muted and less spatially constrained for the $T_{orbital} = 9$ days cases that exhibit the noisiest rainfall signal. In these cases, the hemisphere-integrated top-of-atmosphere outgoing longwave radiation depicted in the phase curves shows no strong correlation with different orbital phases, as shown by the top panels of Figure 9a. This is the result of a more zonally uniform thermal emission from the planet, yielding a more homogeneous signal. In the cases of slower rotation, the disc-integrated top-of-atmosphere outgoing longwave radiation depicted in the light curves show evident asymmetries with respect to the transits/secondary eclipses midpoints. A sinuisoidal curve is clearly identifiable, with evident peaks occurring before the transit phase, during which the entirety of the dark hemisphere is facing the observer. Both emitted light curves shown in the bottom panels of Figure 9a are negatively shifted as a result of the longitudinal asymmetry introduced by the rainfall signal. This negative shift appears to be smaller for the high diffusion case with respect to the low diffusion case, as a consequence of the weaker asymmetry in outgoing longwave radiation at the top of the atmosphere in this scenario due to a weaker rainfall signal (as mentioned in Atmosphere).

Figure 9 highlights the reflected and emitted light variability, by specifically showcasing the 10th and 90th percentiles of the distribution of data from each stellar period, as well as the composite average. As expected, cases of fast rotation present bigger uncertainties, with a significant spread for the thermal emission phase curve. Between the two cases characterized by slow rotation, the low diffusion case is noticeably less noisy, as a con-

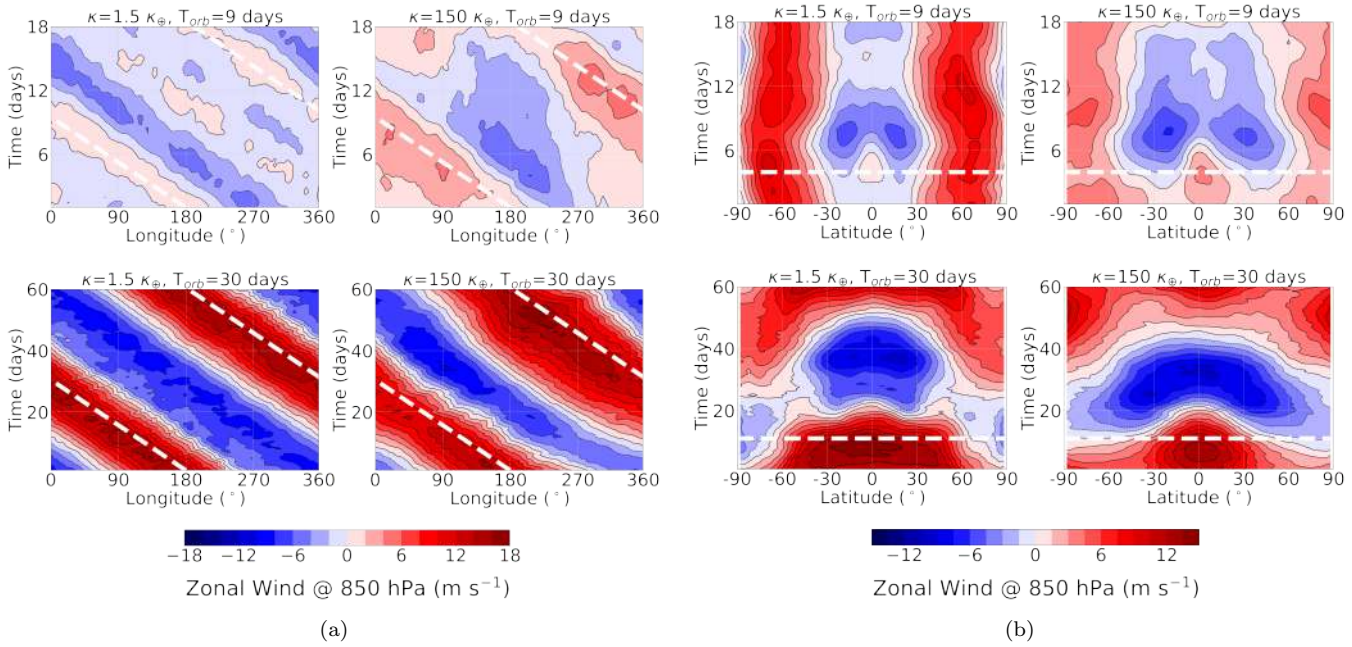

Figure 7: Hovmöller diagram showing composite quantities averaged over the last 100 stellar periods. White dashed lines represent the location of the substellar point. (a) Zonal wind at 850 hPa, averaged over the equatorial band (5°S - 5°N), as a function of longitude. (b) Zonal wind at 850 hPa, at longitude 120°, as a function of latitude.

sequence of the previously mentioned stronger rainfall signal.

The results relative to the thermodynamic ocean simulations, depicted in Figure 9b, show comparable results regarding the reflected light curve. The emitted light curves present asymmetry with respect to the midpoint of the transit, with a comparable shift than their counterparts in Figure 9a. The similarity of these feature indicates that the general climate response is not especially affected by ocean dynamics, and that the surface temperature offset - and therefore rainfall and thermal emission offsets - are a direct consequence of the thermal inertia of the ocean and not a result of horizontal ocean heat transport.

Ocean dynamics plays a role in determining the amplitude of the thermal emission phase curve. In the slow rotation case, the thermodynamic ocean emission phase curve has a slightly larger amplitude with respect to its dynamic counterpart. Compared to the dynamic ocean, the thermodynamic scenario, in which circulation is absent, presents higher temperatures at the equator, but significantly lower temperature at mid- and high- latitudes. This results in lower rainfall and generally more abundant thermal emission. This is especially evident for the higher diffusion case, in which meridional surface temperature gradients are starker.

An additional interesting feature of the emitted light curves depicted in the bottom panels of Figure 9a is the unequal magnitude of successive maxima and minima, as most evidently shown for the case κ=150 $\kappa_\oplus$, $P_{orbital}$ = 30 days. This is a direct consequence of how ocean dynamics interact with the barrier, as this feature is non existent in the thermodynamic counterpart.

More specifically, taking as an example the consecutive maxima of the dynamical case κ=150 $\kappa_\oplus$, $P_{orbital}$ = 30 days, it is evident that the first peak is marginally smaller than the second. Given our observational configuration set up, the orbital phase associated with the first peak corresponds to observing the hemisphere east of the barrier, while the second peak corresponds to observing the hemisphere west of the barrier, with the barrier having just crossed the eastern terminator. The visible hemisphere associated with the first peak exhibits warmer temperatures, a more prominent rainfall and consequently a smaller amount of thermal emission. This is due to the fact that the barrier allows the formation of gyres, that transport heat from the equator to the mid latitudes, analogous to what happens with western boundary currents on Earth (Atkinson 2010).

The time-dependency of the curve amplitude is more evident in the high diffusion case, because the enhanced ocean circulation results in higher mid- and high- latitude surface temperatures compared to the low diffusion scenario, exacerbating the zonal asymmetry introduced by the barrier.

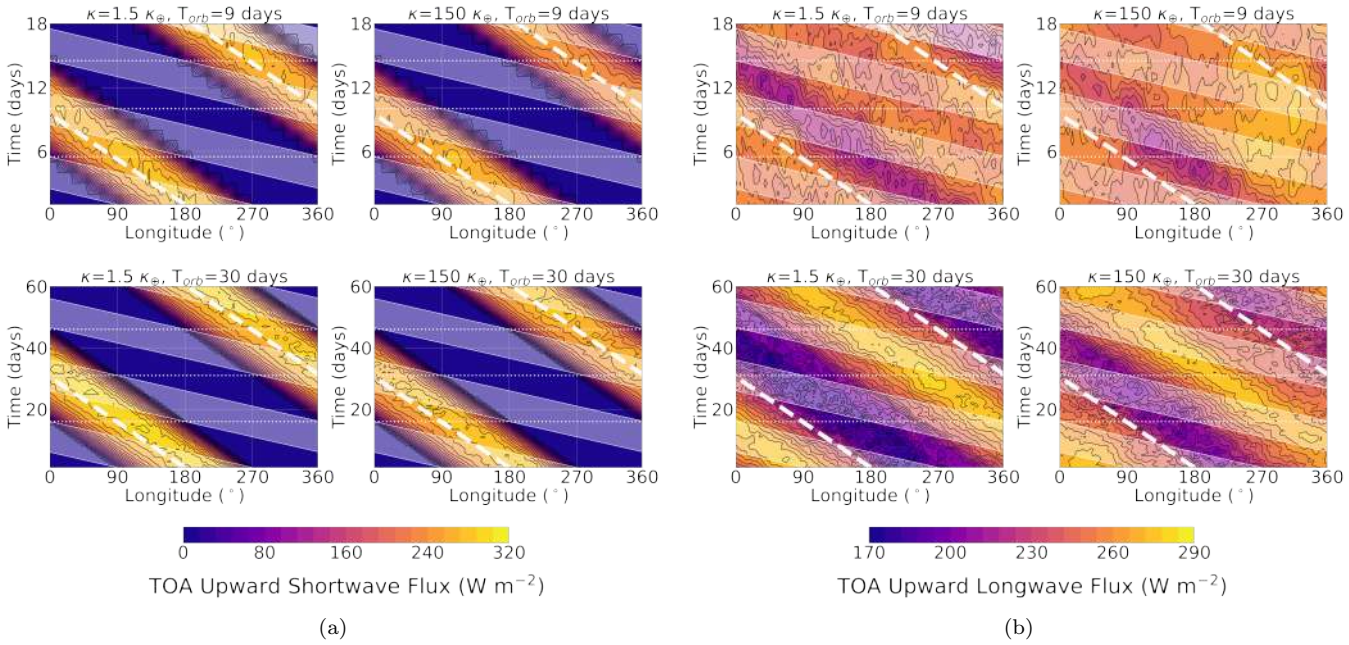

Figure 8: Hovmöller diagram showing composite quantities averaged over the equatorial band (5°S - 5°N) and over the last 100 stellar periods. **White dashed lines represent the location of the substellar point, thin dotted lines correspond to the main phases of transits and secondary eclipses, starting with the first secondary eclipse in all cases. Transparent white stripes indicate the regions of the planet that fall within the observer's field of view, as determined by the system geometry, and correspond to the turquoise hemispheres schematically illustrated in Figure 1. (a) Outgoing shortwave radiation at the top of the atmosphere. The portion of the planet observable in reflected light lies within the transparent white bands on the dayside of the planet, where the TOA upward shortwave flux is non zero. (b) Outgoing longwave radiation at the top of the atmosphere, with the longitudes observable in thermal emission falling within the transparent white bands.**

For both the reflected and emitted light, the thermodynamic ocean simulations present a slightly smaller spread of the 80th percentile compared to the dynamic ocean simulations, consistent with the muted rainfall variability observed in these scenarios, as mentioned in the Atmosphere section.

4. DISCUSSION AND CONCLUSIONS

In this paper we employ a 3D coupled atmosphere-ocean general circulation climate model to investigate climate features of water-rich terrestrial exoplanets captured into 3:2 SORs in the habitable zone of low-mass stars. We explore the interplay between climate, orbital configuration, and therefore rotation regime, and oceanic tidal regime. We address the issue of estimating potential observational characteristics of such planets by analyzing reflectance and thermal emission phase curves, in an effort to establish a criterion that would allow us to discriminate between two possible outcomes of tidal locking - 1:1 and 3:2 SORs - for potentially habitable planets orbiting low-mass stars. This work is primarily motivated by the lack of previous research using a climate model with a dynamic ocean to focus on the evolution of climatic features during a stellar period for planets captured into higher order SORs. While the 1:1 SOR scenario has been extensively studied, 3:2 SOR cases are still relatively unexplored.

The aim of our study is to offer an insight on how both atmosphere and ocean dynamics shape planetary climate and affect potentially observable quantities for the duration of a stellar period in this scenario. In order to present a valuable tool of comparison between two possible SOR scenarios we conducted an idealized study, focusing on varying two parameters - associated with rotation and tidal regimes - of the multidimensional parameter space. This choice resulted in fixing other parameters, such as the stellar radiation forcing at the top of the atmosphere and the orbital eccentricity, to specific values. For instance, the instellation is assumed to be Earth-like, and the orbit is presumed to be circular. While exploring other values of the parameter space would be interesting, it would also be computationally expensive and would introduce multiple degen-

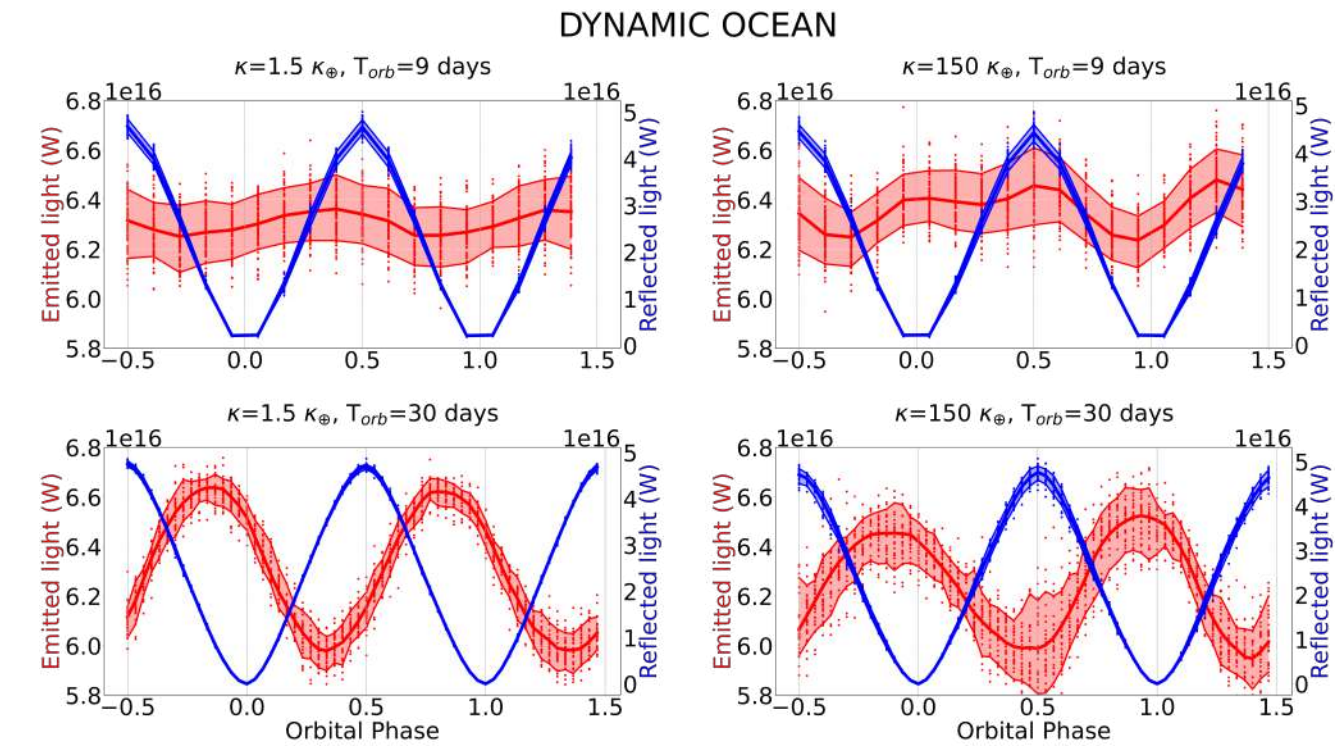

(a)

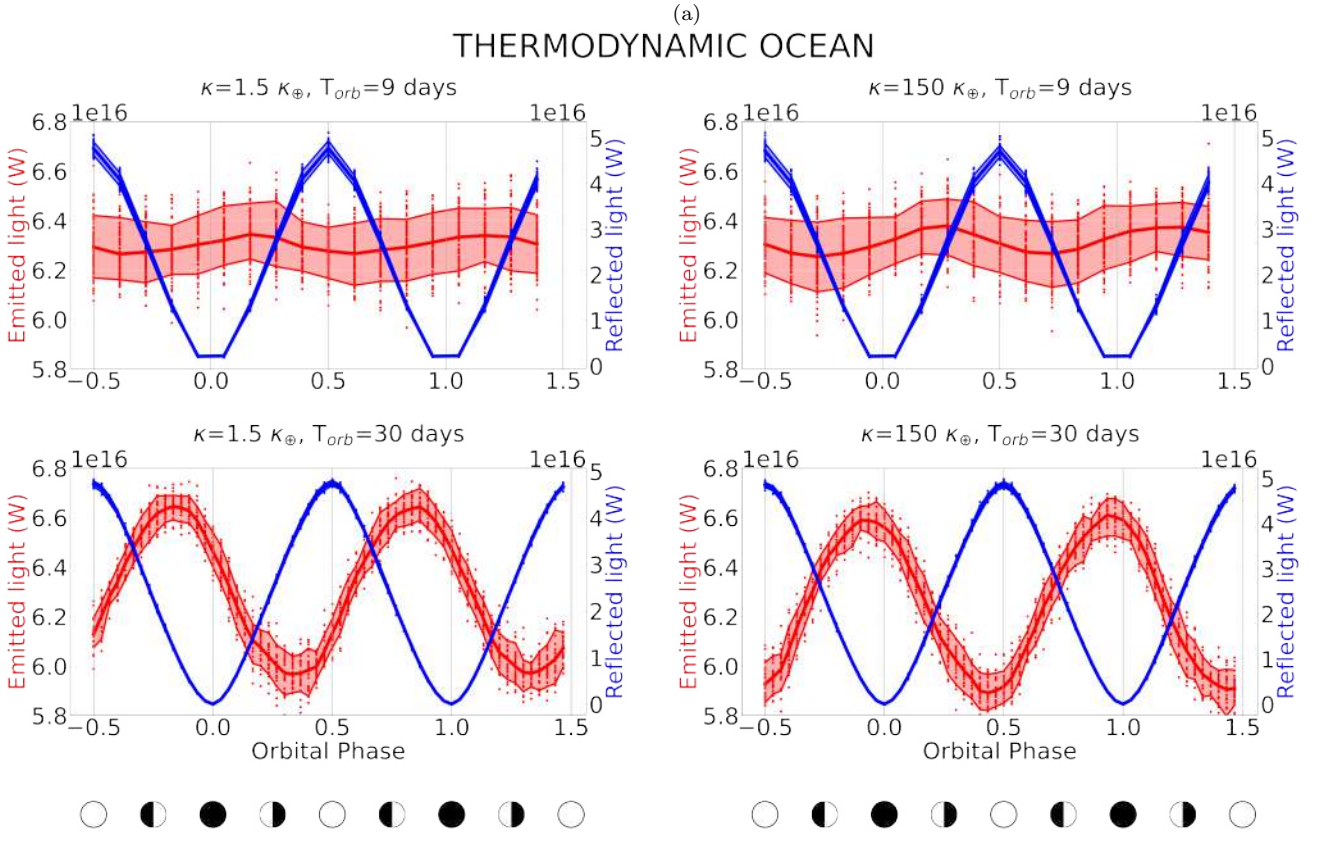

(b)

Figure 9: Emitted and refleced light phase curves for the dynamic ocean scenario (a) and the thermodynamic ocean scenario (b). Scatter plot: daily hemisphere integrated emitted (red) and reflected (blue) flux. Thick line plot: composited emitted (red) and reflected (blue) signal. Shaded region: 10th to 90th percentile range of the emitted (red) and reflected (blue) signal.

eracies that would render a direct comparison of different scenarios more complicated. The choice of a null orbital eccentricity, even if idealized, is particularly convenient, as non-null values would introduce the question of having to additionally establish the planet's longitude at perihelion, introducing yet another dimension to the parameter space. Moreover, the specific choice of adopting a "Ridgeworld" configuration is motivated by the intent of representing a continental setup that would allow a more Earth-like ocean circulation compared to an "Aquaplanet" configuration, while being as general as possible at the same time.

The ocean response is a combination of downward propagating signals and dynamical waves that depend on boundary conditions. Due to the thermal inertia of the ocean, the surface temperature exhibits a 60° longitudinal shift with respect to the position of the substellar point. This results in a similar shift of the position of the maximum rainfall on the planetary surface, with a consequent asymmetry of the thermal emission of the planet, which instead of being centered on the substellar point is shifted westward. This pattern, although present in all analyzed scenarios, is more evident for the slow rotation regime, as the ocean - and consequently the atmosphere - have more time to respond to the heating caused by the slowly shifting stellar forcing. For the same rotation case, tidal scenarios characterized by weaker ocean vertical diffusion present more clearer climate patterns, as the temperature signal resulting from the stellar forcing is not efficiently mixed in the vertical but persists strongly in the upper ocean layers.

In order to fully characterize exoplanetary properties, a combination of thermal emission and reflected light observations would be necessary (Cowan et al. 2012). We simulate phase curves for both emitted and reflected light for all analyzed scenarios, assuming the orbit to be edge-on with respect to a potential observer. Reflected light phase curves do not present any substantial asymmetry with respect to the midpoint of the transit, in any of the analyzed scenarios. Therefore, there is no discernible difference between a 1:1 and a 3:2 scenario, as observed reflected light would peak at full phase (during secondary eclipses) and drop to minima at transits, with no noticeable offset or asymmetry in both cases.

Thermal emission phase curves present more interesting features. The top-of-atmosphere outgoing thermal radiation is a result of the interplay between surface temperature, cloud formation and atmospheric dynamics. In the case of a 1:1 SOR dry exoplanet, with no thick atmosphere, the planet would be characterized by stark thermal contrast between its permanent day and night sides. This would result in a sharp thermal emission peak near secondary eclipse and minimal thermal emission near transit (Koll & Abbot 2015). In the case of a simulated 1:1 SOR exoplanet with a coupled slab ocean, the amplitude of the phase curve would be reduced, as the temperature contrast between the day and the night side would be less stark with respect to the dry case. While the maximum surface temperature coincides with the substellar point, the day hemisphere is shrouded in thick symmetric clouds, which would cause reduced observed thermal emission at the top of the atmosphere. This results in peaks corresponding to transits and troughs corresponding to secondary eclipses (for instance, broadband thermal emission phase curves calculated for temperate aquaplanets shown in Wolf et al. (2019)). These simplified examples of phase curves, shown in the top panels of Figure 10, assume no significant horizontal heat transport - simulated in coarse GCMs with no meridional barriers by unrealistically strong equatorial jets - and no appreciable cloud advection due to strong atmospheric circulation. These would result in a longitudinal shift of the planetary outgoing longwave emission. Moreover, we assume a temperate mean state of the climate, comparable to the one simulated in our cases, and associated with a planet orbiting in the middle range of the habitable zone.

We compare our results, obtained for a 3:2 SOR scenario by employing a coupled atmosphere-ocean general circulation model equipped with a full-depth dynamic ocean, to 1:1 SOR idealized results in Figure 10. We find that both a fast and a slow rotation regime result in phase curves characterized by significantly different features compared with the synchronous rotation scenario, meaning that discerning between the two SORs might be possible from thermal emission observations. In the case of a fast rotation regime, the more homogeneous atmosphere results in a smoother phase curve, with little evidence of peak and troughs. In the case of a slow rotation regime, the longitudinal shift of outgoing longwave radiation as a consequence of the shifted position of the peak in rainfall results in an offset of the thermal emission phase curve. With respect to the 1:1 SOR slab ocean scenario, the phase curve in this case presents a negative shift, with an evident asymmetry with respect to the mid point of the transit. Moreover, the impact of ocean dynamics in combination with a "Ridgeworld" continental configuration results in an orbital phase-dependent amplitude of the curve. The importance of ocean circulation in shaping planetary climates, and therefore potential observables, is evident: this appreciable effect is triggered by a submerged continental barrier, and would undoubtedly be even more pronounced for actual continents, that could introduce

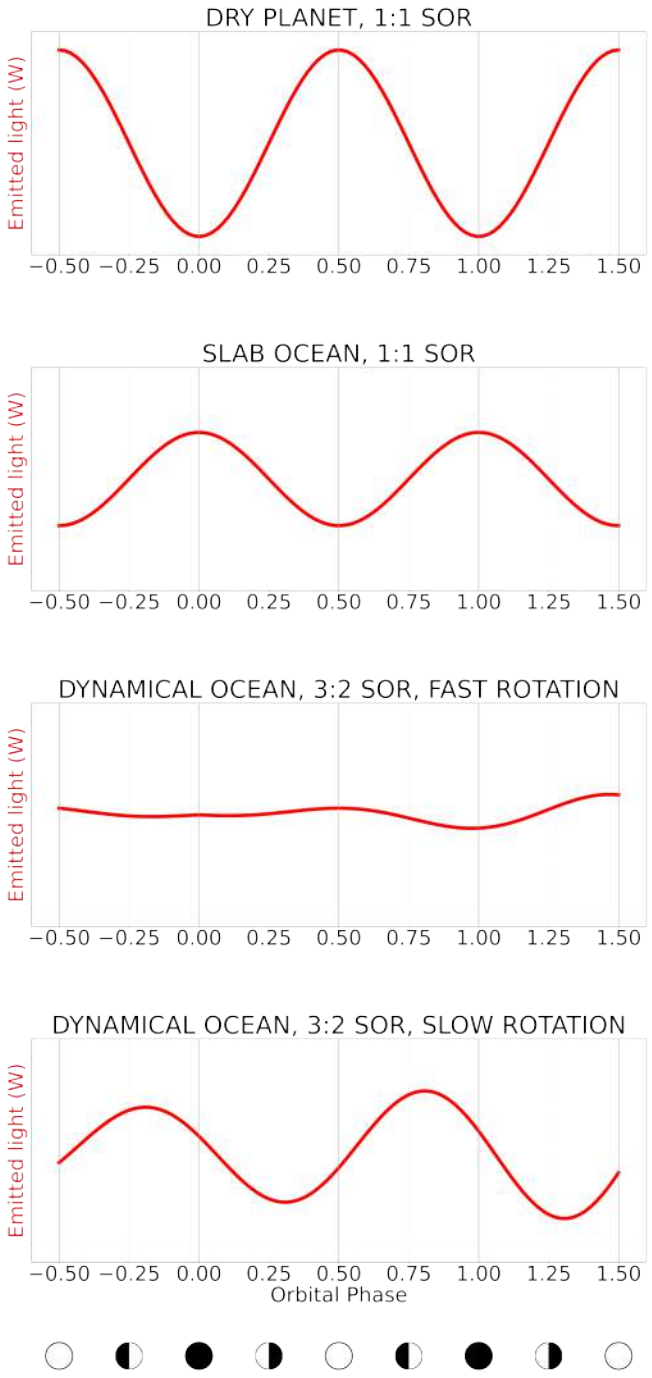

Figure 10: Thermal emission phase curve schematics for idealised 1:1 SOR **- based on previous works, for instance (Koll & Abbot 2015; Wolf et al. 2019) -** and our 3:2 SOR scenarios.

an additional longitudinal asymmetry linked to different surface types.

Climate simulations of similar scenarios differing exclusively for the initial position of the barrier with respect to the substellar point would present the same longitudinal shift in maximum surface temperature, peak rainfall and minimum outgoing longwave radiation. The initial position of the barrier with respect to the observer would influence the shape of the thermal emission phase curve (for instance, the amplitude of consecutive peaks and troughs), but not its offset. This is a consequence of different portions of the planetary surface being in the field of view of the observer. As mentioned in the Observables section, the longitude specific feature of the barrier introduces asymmetries in the planetary thermal emission associated with the same orbital configuration during consecutive orbits.

We note that, although several climate studies regarding 1:1 SOR exoplanets simulate the position of the surface temperature maximum to roughly correspond to the substellar point location, numerous papers have demonstrated how a hot spot offset is highly sensitive to several different factors. Efficient atmospheric/oceanic horizontal heat transport and robust equatorial jet streams can cause an eastward shift of the hot spot with respect to the substellar point (for instance, Hammond & Lewis (2021)). Ocean dynamics influence surface temperatures and atmospheric patterns, and can result in lobster-like spatial pattern instead of eyeball configurations (for instance, (Del Genio et al. 2019)). Various other parameters play an important role in determining climate patterns in this scenario, such as stellar flux, atmospheric composition, planetary rotation rate, surface gravity, planetary radius, and cloud particle size (for instance, Komacek & Abbot (2019)). **An additional factor to consider is the host star spectrum, as the interaction of incident stellar radiation with atmospheric gases and aerosols, and subsequently with the ocean, can potentially affect key climate features and thereby impact both reflected light and thermal phase curves.** The extreme sensitivity not only to the choice of parameter values, but also to physical parameterizations and model architecture complexity and resolution, warrant a vast range of further study of planetary climate states. This issue has prompted the development of a model intercomparison study specifically for synchronous planets orbiting low-mass stars Haqq-Misra et al. (2024), in an ongoing effort to systematically evaluate model performance and achieve a consistent framework that would allow a realistic interpretation of planetary environments from future observational data.

The feasibility of relying on this kind of study to infer information from observational data is still currently under development and is subject to continuous and further refinement. Theoretically, variations in reflectivity and outgoing longwave radiation may be leveraged to distinguish between different orbital configurations.

However, for the case of temperate Earth-sized planets orbiting low-mass stars, this will require the capabilities of the next generation of observatories including the Large Interferometer For Exoplanets (LIFE) (Quanz et al. 2022b) and the Planetary Camera and Spectrograph (PCS) for the Extremely Large Telescope (ELT) (Kasper et al. 2021). We estimate the photometric flux ratio between our simulated planets and an M host star to be $\sim 10^{-8}$, which is above the threshold contrast that the PCS can achieve for hypothetical exo-Earths orbiting nearby M-stars, assuming an adequate angular separation.

The next generation of ground- and space-based observatories have the potential to directly image nearby terrestrial exoplanets residing in the habitable zone of their host star through both thermal emission and reflected light, enabling their characterization. This will allow the atmospheric characterization of a statistically relevant sample of potentially habitable world candidates, which will require the implementation of realistic climate models in order to correctly interpret observational data. In this context, modeling studies such as the one presented in this paper will represent a useful tool develop a theoretical understanding of what future observations might be able to constrain.

ACKNOWLEDGEMENTS

This work was supported by the Engineering and Physical Sciences Research Council (grant number: EP/W524074/1). The research presented in this paper was carried out on the high-performance computing cluster supported by the Research and Specialist Computing Support service at the University of East Anglia.

ORCID IDS

Maria Di Paolo https://orcid.org/0000-0002-0735-2557
David P. Stevens https://orcid.org/0000-0002-7283-4405
Manoj Joshi https://orcid.org/0000-0002-2948-2811

AUTHOR CONTRIBUTIONS STATEMENT

M.D.P., D.S. and M.J. conceived the study. M.D.P. conducted the experiments. All authors contributed to the analysis. All authors reviewed the manuscript.

CODE AND DATA AVAILABILITY

The FORTE2.0 Blaker et al. (2021) code, compilation instructions and example run scripts, together with all necessary ancillary files, are accessible at doi.org/10.5281/zenodo.4108373.

The data that support the findings of this study are accessible at doi.org/10.5281/zenodo.17885048.

REFERENCES

Angerhausen, D., Pidhorodetska, D., Leung, M., et al. 2024, AJ, 167, 128, doi: 10.3847/1538-3881/ad1f4b
Atkinson, L. P. 2010, Western Boundary Currents, ed. K.-K. Liu, L. Atkinson, R. Quiñones, & L. Talaue-McManus (Berlin, Heidelberg: Springer Berlin Heidelberg), 121–169, doi: 10.1007/978-3-540-92735-8_3
Ballard, S., & Johnson, J. A. 2016, ApJ, 816, 66, doi: 10.3847/0004-637X/816/2/66
Barnes, R. 2017, Celestial Mechanics and Dynamical Astronomy, 129, 509, doi: 10.1007/s10569-017-9783-7
Blaker, A. T., Joshi, M., Sinha, B., et al. 2021, Geoscientific Model Development, 14, 275, doi: 10.5194/gmd-14-275-2021
Boutle, I. A., Mayne, N. J., Drummond, B., et al. 2017, A&A, 601, A120, doi: 10.1051/0004-6361/201630020
Braam, M., Palmer, P. I., Decin, L., et al. 2025, PSJ, 6, 5, doi: 10.3847/PSJ/ad9565
Charbonneau, D., & Deming, D. 2007, arXiv e-prints, arXiv:0706.1047, doi: 10.48550/arXiv.0706.1047
Chen, H., Li, G., Paradise, A., & Kopparapu, R. K. 2023, ApJL, 946, L32, doi: 10.3847/2041-8213/acbd33
Cloutier, R., & Menou, K. 2020, AJ, 159, 211, doi: 10.3847/1538-3881/ab8237
Colose, C. M., Haqq-Misra, J., Wolf, E. T., et al. 2021, ApJ, 921, 25, doi: 10.3847/1538-4357/ac135c
Correia, A. C. M., & Delisle, J.-B. 2019, A&A, 630, A102, doi: 10.1051/0004-6361/201936336
Correia, A. C. M., & Laskar, J. 2009, Icarus, 201, 1, doi: 10.1016/j.icarus.2008.12.034
Cowan, N. B., Voigt, A., & Abbot, D. S. 2012, ApJ, 757, 80, doi: 10.1088/0004-637X/757/1/80
Cullum, J., Stevens, D., & Joshi, M. 2014, Astrobiology, 14, 645, doi: 10.1089/ast.2014.1171
Del Genio, A. D., Way, M. J., Amundsen, D. S., et al. 2019, Astrobiology, 19, 99, doi: 10.1089/ast.2017.1760
Di Paolo, M., Stevens, D. P., Joshi, M., & Hall, R. A. 2025, ApJL, 982, L48, doi: 10.3847/2041-8213/adbca3
Dobrovolskis, A. R. 2007, Icarus, 192, 1, doi: 10.1016/j.icarus.2007.07.005
—. 2015, Icarus, 250, 395, doi: 10.1016/j.icarus.2014.12.017
Dressing, C. D., & Charbonneau, D. 2013, ApJ, 767, 95, doi: 10.1088/0004-637X/767/1/95
—. 2015, ApJ, 807, 45, doi: 10.1088/0004-637X/807/1/45

Fang, J., & Margot, J.-L. 2013, ApJ, 767, 115, doi: 10.1088/0004-637X/767/2/115
Ferreira, D., Marshall, J., & Campin, J.-M. 2010, Journal of Climate, 23, 1456, doi: 10.1175/2009JCLI3197.1
Ferreira, D., Marshall, J., O'Gorman, P. A., & Seager, S. 2014, Icarus, 243, 236, doi: 10.1016/j.icarus.2014.09.015
Forster, P. M., Blackburn, M., Glover, R., & Shine, K. P. 2000, Climate Dynamics, 16, 833, doi: 10.1007/s003820000083
Goldreich, P. 1965, Nature, 208, 375, doi: 10.1038/208375b0
—. 1966, AJ, 71, 1, doi: 10.1086/109844
Goldreich, P., & Peale, S. 1966a, AJ, 71, 425, doi: 10.1086/109947
Goldreich, P., & Peale, S. J. 1966b, Nature, 209, 1117, doi: 10.1038/2091117a0
Hadden, S., & Lithwick, Y. 2017, AJ, 154, 5, doi: 10.3847/1538-3881/aa71ef
Hammond, M., & Lewis, N. T. 2021, Proceedings of the National Academy of Science, 118, e2022705118, doi: 10.1073/pnas.2022705118
Hammond, T., & Komacek, T. D. 2024, ApJ, 968, 43, doi: 10.3847/1538-4357/ad4a59
Haqq-Misra, J., Wolf, E. T., Fauchez, T. J., Shields, A. L., & Kopparapu, R. K. 2024, PSJ, 5, 169, doi: 10.3847/PSJ/ad5dae
Haqq-Misra, J., Wolf, E. T., Joshi, M., Zhang, X., & Kopparapu, R. K. 2018, ApJ, 852, 67, doi: 10.3847/1538-4357/aa9f1f
Harada, C. K., Dressing, C. D., Kane, S. R., & Ardestani, B. A. 2024, ApJS, 272, 30, doi: 10.3847/1538-4365/ad3e81
Harwit, M. 1998, "Stars - Sources of Stellar Energy" in Astrophysical concepts (Astronomy and astrophysics library, Springer), 290–292
Herweijer, C., Seager, R., Winton, M., & Clement, A. 2005, Tellus Series A, 57, 662, doi: 10.3402/tellusa.v57i4.14708
Hu, Y., & Yang, J. 2014, Proceedings of the National Academy of Science, 111, 629, doi: 10.1073/pnas.1315215111
Joshi, M., Stringer, M., van der Wiel, K., O'Callaghan, A., & Fueglistaler, S. 2015, Geoscientific Model Development, 8, 1157, doi: 10.5194/gmd-8-1157-201510.5194/gmdd-7-5517-2014
Joshi, M. M., & Haberle, R. M. 2012, Astrobiology, 12, 3, doi: 10.1089/ast.2011.0668
Joshi, M. M., Haberle, R. M., & Reynolds, R. T. 1997, Icarus, 129, 450, doi: 10.1006/icar.1997.5793
Kasper, M., Cerpa Urra, N., Pathak, P., et al. 2021, The Messenger, 182, 38, doi: 10.18727/0722-6691/5221
Kasting, J. F., Whitmire, D. P., & Reynolds, R. T. 1993, Icarus, 101, 108, doi: 10.1006/icar.1993.1010
Kienert, H., Feulner, G., & Petoukhov, V. 2012, Geophys. Res. Lett., 39, L23710, doi: 10.1029/2012GL054381
Kilic, C., Lunkeit, F., Raible, C. C., & Stocker, T. F. 2018, ApJ, 864, 106, doi: 10.3847/1538-4357/aad5eb
Kilic, C., Raible, C. C., & Stocker, T. F. 2017, ApJ, 844, 147, doi: 10.3847/1538-4357/aa7a03
Koll, D. D. B., & Abbot, D. S. 2015, ApJ, 802, 21, doi: 10.1088/0004-637X/802/1/21
Komacek, T. D., & Abbot, D. S. 2019, ApJ, 871, 245, doi: 10.3847/1538-4357/aafb33
Kopparapu, R. k., Wolf, E. T., Arney, G., et al. 2017, ApJ, 845, 5, doi: 10.3847/1538-4357/aa7cf9
Kopparapu, R. k., Wolf, E. T., Haqq-Misra, J., et al. 2016, ApJ, 819, 84, doi: 10.3847/0004-637X/819/1/84
Kopparapu, R. K., Ramirez, R., Kasting, J. F., et al. 2013, ApJ, 765, 131, doi: 10.1088/0004-637X/765/2/131
Leconte, J., Wu, H., Menou, K., & Murray, N. 2015, Science, 347, 632, doi: 10.1126/science.1258686
MacDonald, G. J. F. 1964, Reviews of Geophysics and Space Physics, 2, 467, doi: 10.1029/RG002i003p00467
Ment, K., & Charbonneau, D. 2023, AJ, 165, 265, doi: 10.3847/1538-3881/acd175
Munk, W., & Wunsch, C. 1998, Deep Sea Research Part I: Oceanographic Research, 45, 1977, doi: 10.1016/S0967-0637(98)00070-3
Murray, C. D., & Dermott, S. F. 1999, "Tides, Rotation, and Shape" in Solar System Dynamics (Cambridge University Press), 130–135, doi: 10.1017/CBO9781139174817
Nowajewski, P., Rojas, M., Rojo, P., & Kimeswenger, S. 2018, Icarus, 305, 84, doi: 10.1016/j.icarus.2018.01.002
Olson, S. L., Jansen, M., & Abbot, D. S. 2020, ApJ, 895, 19, doi: 10.3847/1538-4357/ab88c9
Pierrehumbert, R. T. 2011, ApJL, 726, L8, doi: 10.1088/2041-8205/726/1/L8
Quanz, S. P., Absil, O., Benz, W., et al. 2022a, Experimental Astronomy, 54, 1197, doi: 10.1007/s10686-021-09791-z
Quanz, S. P., Ottiger, M., Fontanet, E., et al. 2022b, A&A, 664, A21, doi: 10.1051/0004-6361/202140366
Ragon, C., Vérard, C., Kasparian, J., & Brunetti, M. 2024, Scientific Reports, 14, 26136, doi: 10.1038/s41598-024-76432-8
Renaud, J. P., Henning, W. G., Saxena, P., et al. 2021, PSJ, 2, 4, doi: 10.3847/PSJ/abc0f3
Ribas, I., Bolmont, E., Selsis, F., et al. 2016, A&A, 596, A111, doi: 10.1051/0004-6361/201629576

Scalo, J., Kaltenegger, L., Segura, A., et al. 2007, Astrobiology, 7, 85, doi: 10.1089/ast.2006.0125

Schmidt, F., Way, M. J., Costard, F., et al. 2022, Proceedings of the National Academy of Science, 119, e2112930118, doi: 10.1073/pnas.2112930118

Shields, A. L., Ballard, S., & Johnson, J. A. 2016, PhR, 663, 1, doi: 10.1016/j.physrep.2016.10.003

Shields, A. L., Meadows, V. S., Bitz, C. M., et al. 2013, Astrobiology, 13, 715, doi: 10.1089/ast.2012.0961

Smith, R. S., Dubois, C., & Marotzke, J. 2006, Journal of Climate, 19, 4719, doi: 10.1175/JCLI3874.1

Trenberth, K. E., & Caron, J. M. 2001, Journal of Climate, 14, 3433, doi: 10.1175/1520-0442(2001)014⟨3433:EOMAAO⟩2.0.CO;2

Turbet, M., Leconte, J., Selsis, F., et al. 2016, A&A, 596, A112, doi: 10.1051/0004-6361/201629577

Valente, E. F. S., Correia, A. C. M., Auclair-Desrotour, P., Farhat, M., & Laskar, J. 2024, A&A, 687, A47, doi: 10.1051/0004-6361/202348450

van de Velde, S. J., Hülse, D., Reinhard, C. T., & Ridgwell, A. 2021, Geoscientific Model Development, 14, 2713, doi: 10.5194/gmd-14-2713-2021

Van Eylen, V., & Albrecht, S. 2015, ApJ, 808, 126, doi: 10.1088/0004-637X/808/2/126

Vinson, A. M., & Hansen, B. M. S. 2017, MNRAS, 472, 3217, doi: 10.1093/mnras/stx2100

Wang, Y., Tian, F., & Hu, Y. 2014, ApJL, 791, L12, doi: 10.1088/2041-8205/791/1/L12

Way, M. J., & Del Genio, A. D. 2020, Journal of Geophysical Research (Planets), 125, e06276, doi: 10.1029/2019JE00627610.1002/essoar.10501118.3

Webb, D. J. 1996, Computers and Geosciences, 22, 569, doi: 10.1016/0098-3004(95)00133-6

Winton, M. 2003, Journal of Climate, 16, 2875, doi: 10.1175/1520-0442(2003)016⟨2875:OTCIOO⟩2.0.CO;2

Wolf, E. T., Kopparapu, R. K., & Haqq-Misra, J. 2019, ApJ, 877, 35, doi: 10.3847/1538-4357/ab184a

Wu, Y., & Lithwick, Y. 2013, ApJ, 772, 74, doi: 10.1088/0004-637X/772/1/74

Yang, J., Abbot, D. S., Koll, D. D. B., Hu, Y., & Showman, A. P. 2019, ApJ, 871, 29, doi: 10.3847/1538-4357/aaf1a8

Yang, J., Cowan, N. B., & Abbot, D. S. 2013, ApJL, 771, L45, doi: 10.1088/2041-8205/771/2/L45

Yang, J., Ji, W., & Zeng, Y. 2020, Nature Astronomy, 4, 58, doi: 10.1038/s41550-019-0883-z

Yang, J., Peltier, W. R., & Hu, Y. 2012a, Journal of Climate, 25, 2711, doi: 10.1175/JCLI-D-11-00189.1

—. 2012b, Journal of Climate, 25, 2737, doi: 10.1175/JCLI-D-11-00190.1

Yuan, H. D. A., Su, Y., & Goodman, J. 2025, ApJ, 987, 9, doi: 10.3847/1538-4357/add2f3

Zúñiga-Fernández, S., Gillon, M., Pedersen, P. P., et al. 2024, in Society of Photo-Optical Instrumentation Engineers (SPIE) Conference Series, Vol. 13094, Ground-based and Airborne Telescopes X, ed. H. K. Marshall, J. Spyromilio, & T. Usuda, 1309413, doi: 10.1117/12.3020550